ACS APPLIED MATERIALS & INTERFACES

Research Article

www.acsami.org

Magnetic Properties of Single Crystalline Expanded Austenite Obtained by Plasma Nitriding of Austenitic Stainless Steel Single Crystals

Enric Menéndez,[*,†,‡] Claude Templier,[*,§] Pablo Garcia-Ramirez,[‡,⊥] José Santiso,[‡,⊥] André Vantomme,[†] Kristiaan Temst,[†] and Josep Nogués[‡,#]

[†]Instituut voor Kern- en Stralingsfysica, KU Leuven, Celestijnenlaan 200 D, B-3001 Leuven, Belgium

[‡]ICN2 - Institut Catala de Nanociencia i Nanotecnologia, Campus UAB, 08193 Bellaterra, Barcelona, Spain

[§]Institut P′, Université de Poitiers & ENSMA, 86962 Futuroscope-Chasseneuil, France

[⊥]CSIC - Consejo Superior de Investigaciones Cientificas, ICN2 Building, 08193 Bellaterra, Barcelona, Spain

[#]ICREA - Institució Catalana de Recerca i Estudis Avançats, 08010 Barcelona, Spain

ABSTRACT: Ferromagnetic single crystalline [100], [110], and [111]-oriented expanded austenite is obtained by plasma nitriding of paramagnetic 316L austenitic stainless steel single crystals at either 300 or 400 °C. After nitriding at 400 °C, the [100] direction appears to constitute the magnetic easy axis due to the interplay between a large lattice expansion and the expected decomposition of the expanded austenite, which results in Fe- and Ni-enriched areas. However, a complex combination of uniaxial (i.e., twofold) and biaxial (i.e., fourfold) in-plane magnetic anisotropies is encountered. It is suggested that the former is related to residual stress-induced effects while the latter is associated to the in-plane projections of the cubic lattice symmetry. Increasing the processing temperature strengthens the biaxial in-plane anisotropy in detriment of the uniaxial contribution, in agreement with a more homogeneous structure of expanded austenite with lower residual stresses. In contrast to polycrystalline expanded austenite, single crystalline expanded austenite exhibits its magnetic easy axes along basic directions.

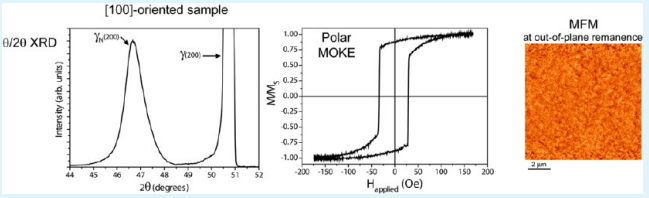

KEYWORDS: *austenitic stainless steel, single crystal, nitriding, expanded austenite, ferromagnetism, structure−property relationships*

INTRODUCTION

Austenitic stainless steels (ASSs) exhibit an interesting combination of structural and magnetic properties. Whereas ASSs are paramagnetic at room temperature,[1−3] they become partly ferromagnetic after nitriding[4,5] at moderate temperatures (e.g., ≈400 °C) by means of the formation of the so-called expanded austenite γ_N phase.[6] Namely, since the threshold for ferromagnetism requires a certain minimum of nitrogen concentration, not the whole nitrided layer is ferromagnetic, rendering two magnetically dissimilar parts (one paramagnetic and the other ferromagnetic) depending on the nitrogen concentration along the depth.[4] In fact, rather than a supersaturated nitrogen solid solution, recent studies indicate a multiphase nature of expanded austenite, consisting of nanometric CrN precipitates embedded in a Fe_4N-like matrix.[7] Nitriding widens the fields of application of ASSs not only from a magnetic point of view but also from a mechanical side, leading to an enhanced hardness[8] and wear resistance[9] without compromising corrosion resistance.[4] This phase transformation brings about additional prospective functionalities such as remote magnetic detection of the presence of the otherwise non-ferromagnetic ASSs, easy movement and transport of ASS pieces using magnetic fields or enabling ASSs as potential candidates for magnetic patterning applications. Ion beam nitriding[10] and plasma nitriding[11] through shadow masks have already been used to locally generate ferromagnetic structures embedded in a paramagnetic matrix. Specifically, both in-plane[10] and out-of-plane[11] magnetization have been demonstrated in these magnetic patterning approaches. Even though attempts to unravel the orientation-dependent magnetic properties (such as the effective easy and hard axes) of expanded austenite have been recently performed in plasma-nitrided polycrystalline ASSs (i.e., polycrystalline γ_N),[11] so far little is known about the intrinsic magnetic properties of expanded austenite. The interplay among magnetocrystalline anisotropy and exchange, dipolar, and mechanical interactions between grains plays a significant role in determining the effective magnetic properties of polycrystalline expanded austenite. In this context, a study of the magnetic properties of single crystalline expanded austenite (i.e., γ_N with no grain to grain interaction due to the virtual lack of grain boundaries) is of particular interest. Following this, we present a detailed study on the tentative correlation between the crystalline orientation

Received: July 11, 2013
Accepted: September 12, 2013
Published: September 12, 2013

and the magnetic properties of single crystalline expanded austenite.

RESULTS AND DISCUSSION

Structural Characterization of Single Crystalline Expanded Austenite. In agreement with literature,[12−14] nuclear reaction analysis (NRA) nitrogen depth profiles show a quasi-linear decrease followed by a sharp leading edge (Figure 1a). The thickness of the nitrided layer depends on the crystalline orientation with the [100] orientation being most favorable for nitrogen diffusion.[12,15,16] In addition, plasma nitriding at 400 °C results in roughly twice as thick nitrided layers compared to those nitrided at 300 °C. Note that the apparent lower near-surface N concentration of the samples nitrided at 300 °C can be partly an artifact of the low depth resolution of NRA (≈0.1 μm near the surface): a steep N concentration decrease close to the surface (like those exhibited by the samples nitrided at 300 °C) gives an averaged value slightly lower than the top surface concentration.

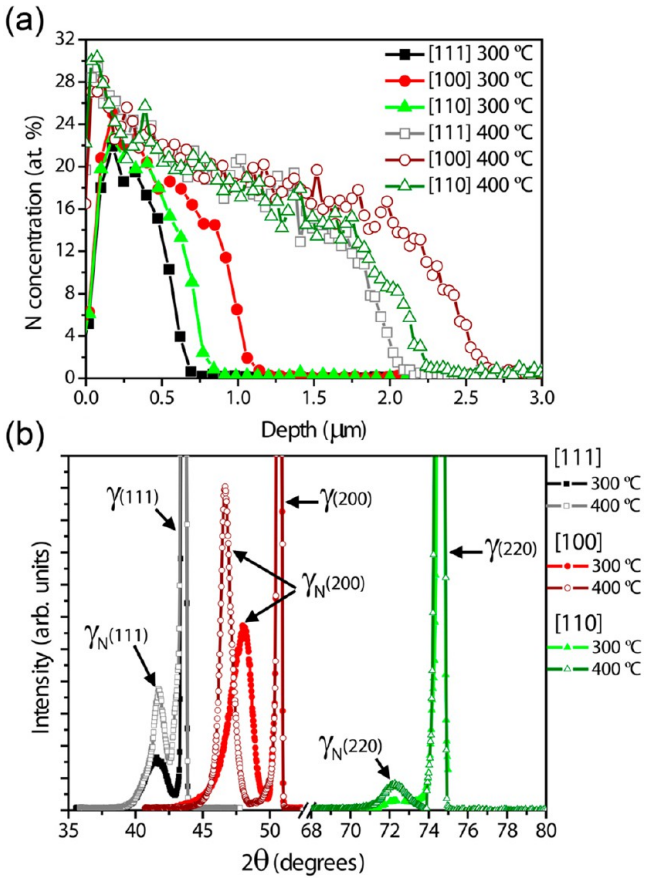

Figure 1. Structural properties of plasma-nitrided ASSs: (a) NRA nitrogen depth profiles and (b) symmetric $\theta/2\theta$ XRD patterns (the XRD data are normalized to the maximum intensity of the austenite lines).

The structure of the pristine ASS single crystals is consistent with a fully textured face centered cubic (FCC) lattice of the γ austenite phase as revealed by the symmetric $\theta/2\theta$ X-ray diffraction (XRD) patterns (Figure 1b). After nitriding, each γ XRD peak exhibits a satellite peak located at lower diffraction angles which corresponds to the γ_N phase. The absence of other crystallographic γ_N peaks already suggests that this phase preserves the orientation of the parent γ phase after nitriding. The γ_N peaks are rather asymmetric, in particular those corresponding to the samples produced at 300 °C. This is mostly due to the inhomogeneous N depth distribution and consequent compressive residual stress gradient in the nitrided layer.[4,17,18] Under symmetric 2θ scans, while XRD roughly probes the top 4−6 μm depending on the crystalline orientation, most of the intensity of the diffraction peaks comes roughly from the first micrometer because of absorption,[19,20] leading to a larger percentage of the γ_N phase in the diffracting volume after nitriding at 400 °C than at 300 °C. This results in an increase of the intensity of the γ_N peaks at the expense of the γ peaks (Figure 1b). Concomitantly, sharpening and gain of symmetry of the γ_N XRD peaks are also observed. This can be ascribed to better crystalline quality and homogeneity of the γ_N phase since interstitial diffusion and stress relaxation via plastic deformation processes are enhanced at higher temperatures. Therefore, from a structural point of view, nitriding at 400 °C might lead to a more relaxed expanded austenite than at 300 °C. This is in agreement with previously reported results.[21,22] However, it should be taken into account that, given the limited X-ray penetration and the deeper N penetration for the 400 °C samples, XRD probes a less pronounced N gradient for these samples.

To further assess the degree of texture of both the austenite and the expanded austenite phases and to reveal their crystallographic relationship, asymmetric Φ scans have been carried out and mapped while varying χ (Figure 2). Diffraction conditions are achieved by choosing the diffracting angle of the phase and planes of interest. The γ and γ_N peaks are located at almost identical Φ values. For instance, the (220) planes of the austenite and the expanded austenite produced at either 300 °C or 400 °C in the [100]-oriented samples are virtually parallel. The equal number of peaks evidences that the expanded austenite shows a FCC-like structure (i.e., same crystal symmetry) in agreement with the fact that the nitrided region retains roughly the structure of the host austenite.[6,23] The slight deviation in Φ observed for the [110] samples might be somewhat linked to the lattice rotations observed in the ⟨110⟩ oriented grains of plasma-nitrided polycrystalline ASS 316L.[24,25] This might also explain the rather weak intensity of the 220 γ_N peaks in Figure 1b. Nitriding of polycrystalline samples results in a rotation of the expanded austenite lattice with respect to the initial crystalline orientation. The amount and direction of these crystallographic plane rotations within the nitrided layer depend mainly on the initial orientation of the surface (i.e., the nature of the planes parallel to the surface). While the {111} and {200} planes hardly change, the {220} ones do.[24,25]

Rocking curves (not shown) indicate a low degree of mosaicity, i.e., narrow distribution of misorientation angles among unit cells. Specifically, while the full width at half maximum for austenite peaks is around 0.7°, it is in the range of 1.5−2.5° and 1.0−1.5° for the expanded austenite produced at 300 °C and 400 °C, respectively. This evidences again the role of thermal activation in achieving an expanded austenite layer with weaker gradients and higher degree of crystallinity for the same nitriding duration.

Table 1 gives the interplanar distances of the (111), (200), and (220) planes of the expanded austenite produced at either 300 or 400 °C corresponding to planes either parallel (from symmetric XRD scans) or tilted (from asymmetric XRD scans) with respect to the sample surface. The apparent relative

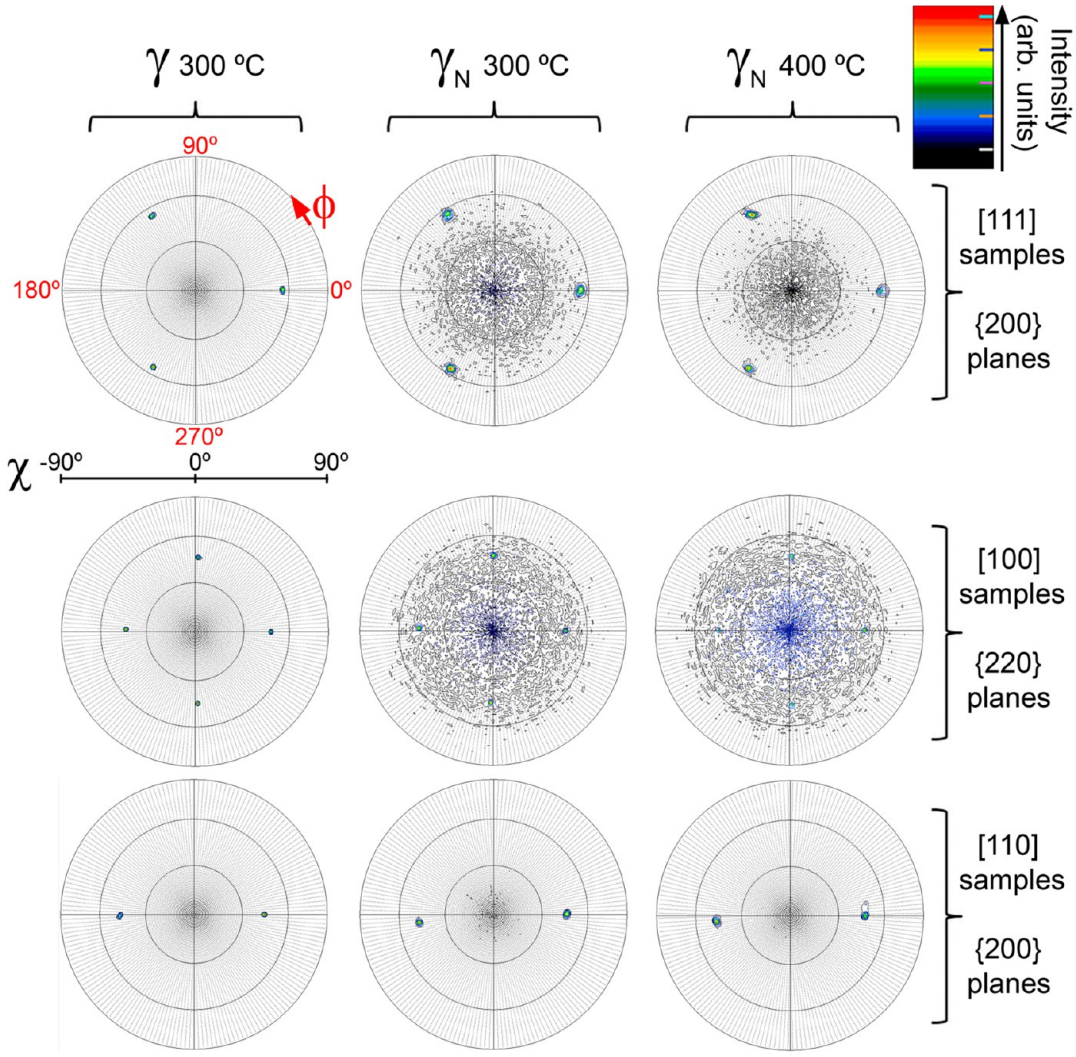

Figure 2. Pole figures (i.e., stereographic projection of $\Phi-\chi$ area scans) at the diffraction conditions of the planes of interest: 200 reflection for [111] and [110]-oriented samples (first and third rows) and 220 for [100]-oriented samples (second row) corresponding to the austenite phase of the sample treated at 300 °C (first column) and to the expanded austenite phase produced at 300 °C (second column) and at 400 °C (third column).

Table 1. Interplanar Spacings d_{hkl} and Their Related Apparent Relative Expansions Corresponding to the (111), (200), and (220) Planes of the Obtained Expanded Austenite Phases Assessed by Means of Both Symmetric ($\chi = 0°$) and Asymmetric $\theta/2\theta$ XRD Scans ($\chi \neq 0°$): From Symmetric (†, Figure 1) and/or asymmetric (§, Figure 3) $\theta/2\theta$ XRD Scans[a]

sample		*hkl* reflection	χ [deg]	$\theta_{hkl} \pm 0.001$ [deg]	d_{hkl} [nm]	$\Delta d_{hkl}/d_{hkl}$ [%]
300 °C	[100]	200	0	24.023	$0.189 \pm 0.008^{\dagger,\S}$	5.3 ± 0.5
		220	44.32	35.861	0.131 ± 0.004	3.5 ± 0.3
		111	57.67	20.745	0.218 ± 0.011	4.8 ± 0.6
300 °C	[110]	220	0	36.196	$0.130 \pm 0.004^{\dagger}$	2.6 ± 0.3
		200	46.88	24.047	$0.189 \pm 0.008^{\S}$	5.2 ± 0.5
300 °C	[111]	111	0	20.753	$0.217 \pm 0.011^{\dagger}$	4.7 ± 0.6
		200	54.68	24.331	$0.187 \pm 0.008^{\S}$	4.0 ± 0.5
400 °C	[100]	200	0	23.348	$0.194 \pm 0.009^{\dagger,\S}$	8.2 ± 0.5
		220	46.93	36.103	0.131 ± 0.004	2.8 ± 0.3
		111	55.23	20.726	0.218 ± 0.012	4.9 ± 0.6
400 °C	[110]	220	0	36.167	$0.131 \pm 0.004^{\dagger}$	2.8 ± 0.3
		200	47.29	24.012	$0.189 \pm 0.008^{\S}$	5.3 ± 0.5
400 °C	[111]	111	0	20.865	$0.216 \pm 0.011^{\dagger}$	4.2 ± 0.5
		200	55.86	24.354	$0.187 \pm 0.008^{\S}$	3.9 ± 0.5

[a]Note that the calculated expansions do not take into account the shifts resulting from faulting.

expansions $\Delta d_{hkl}/d_{hkl} = (d_{hkl}(\gamma_N) - d_{hkl}(\gamma))/d_{hkl}(\gamma))$ are quantified with respect to the pristine austenite using the interplanar distances obtained from the symmetric scans: $d_{200}(\gamma) = 0.1798$ nm, $d_{220}(\gamma) = 0.1271$ nm, and $d_{111}(\gamma) =$

0.2075 nm. Since the expanded austenite peaks of samples produced at 300 °C are rather asymmetric, the presented Bragg angles are those corresponding to their maximum intensity. Note that while the symmetric scans provide out-of-plane structural information, the asymmetric measurements account for structural parameters corresponding to planes tilted with respect to the sample surface, partially providing in-plane structural characteristics. Given the different N penetration between the 300 and 400 °C samples and the limited XRD probed depth (the first 1−1.5 and 0.8−1.2 μm depending on the crystalline orientation determine roughly the major part of the diffraction lines in symmetric and asymmetric XRD measurements, respectively),[19,20] caution should be taken when comparing $\Delta d_{hkl}/d_{hkl}$ values for the two different processing temperatures. However, for a given temperature, it is rather plausible to compare the XRD results for dissimilar crystalline orientations since the probed volumes exhibit a similar N depth profile.

As can also be seen in the symmetric XRD scans of Figure 1b, the (200) planes of γ_N seem to expand more than the (111) and (220) planes ($\Delta d_{200}/d_{200}(\gamma) > \Delta d_{111}/d_{111}(\gamma) > \Delta d_{220}/d_{220}(\gamma)$, see Table 1), and this apparent expansion becomes more prominent with temperature in agreement with previously reported results.[6,26,27] Figure 3 shows the asymmetric (i.e., $\chi \neq 0°$) and symmetric (i.e., $\chi = 0°$) XRD scans corresponding to the 200 reflection of the expanded austenite phases for both temperatures. While the (200) XRD peaks of samples produced at 300 °C are highly asymmetric, those of samples produced at 400 °C are fairly symmetric, evidencing the larger percentage of the γ_N phase in the diffracting volume for samples produced at 400 °C. Interestingly, given a processing temperature, the XRD peak shifts are less pronounced as the (200) planes are more tilted with respect to the sample surface (e.g., from 8.2 down to 3.9% as χ varies from 0 to 55.86° for the samples treated at 400 °C, Table 1). This trend is in agreement with the presence of in-plane biaxial residual stresses in the nitrided layer, which induce a negative (i.e, compressive) elastic strain parallel to the surface and a positive (i.e., tensile) elastic strain in the normal direction.[28] In contrast to (200) planes, (110) and (111) planes exhibit a more isotropic expansion independently from their initial orientation with respect to the sample surface, suggesting that the influence of the residual stresses appears to be more effective on the (200) planes, evidencing the strong anisotropy of the elastic properties along these planes.[29] Hence, a tetragonal-like or other distortion from a FCC, with a height c along [100] slightly larger than the length of a square-like base (i.e., $c > a,b$ with $a \approx b$), could roughly give a plausible explanation of the structural nature of [100] and [110]-oriented expanded austenite.[13] As can be seen in Table 1, the apparent relative expansion of (200) planes of the [110]-oriented sample is significantly larger than the out-of-plane expansion of (220) planes for both processing temperatures. Nonetheless, for the [111]-oriented expanded austenite, a regular FCC structure with expanded lattice parameter would be a more reasonable structure since the apparent relative expansion of the (200) planes is rather similar to the out-of-plane expansion of the (111) planes for both processing temperatures, evidencing its more isotropic crystalline character. Therefore, the manifestation and the type of the crystalline distortion depends on the pristine orientation of crystalline planes with respect to the surface.[13] This also agrees with the description of the γ_N structure made by Christiansen et al. as a faulted and stressed FCC phase.[29]

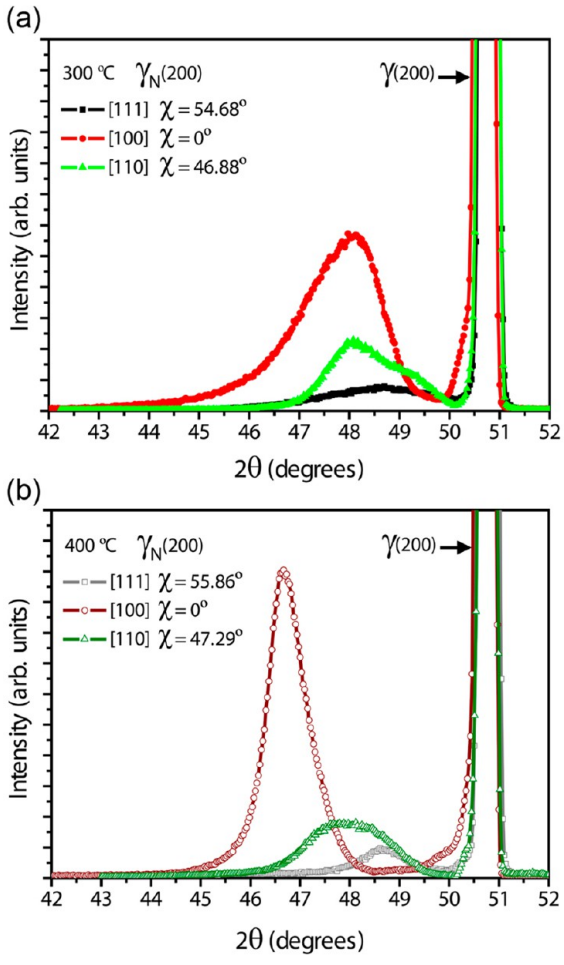

Figure 3. Symmetric XRD $\theta/2\theta$ scans ($\chi = 0°$) of the [100]-oriented samples and asymmetric XRD $\theta/2\theta$ scans ($\chi \neq 0°$) of the [111] and [110]-oriented samples to investigate the (200) planes of the expanded austenite produced at 300 °C (a) and at 400 °C (b).

Magnetic Properties of Single Crystalline Expanded Austenite. *Out-of-Plane Magnetic Characterization.* The pristine 316L ASS single crystals show no ferromagnetic signal by either polar or longitudinal magneto-optical Kerr effect (MOKE) (not shown), confirming their paramagnetic character. Nonetheless, after nitriding at either 300 or 400 °C, the samples become ferromagnetic, evidencing the formation of expanded austenite. It is worth mentioning that since MOKE is a surface sensitive technique which probes the first few tens of nanometers, the effect of the nitrogen concentration profile on the obtained magnetic results is minimized.

Figure 4 shows the out-of-plane MOKE hysteresis loops for the three samples treated at 300 °C, revealing that the [110]-oriented sample has the hard magnetic axis out-of-plane; i.e., its hysteresis loop exhibits almost vanishing remanence and coercivity (Table 2). The [100] and [111] 300 °C-samples do not have well established easy or hard axes out-of-plane. Conversely, the samples prepared at 400 °C show an increased out-of-plane component in comparison to the samples treated at 300 °C. In particular, the [100] expanded austenite exhibits a rather square-shaped loop, evidenced by a high remanence value (Table 2).

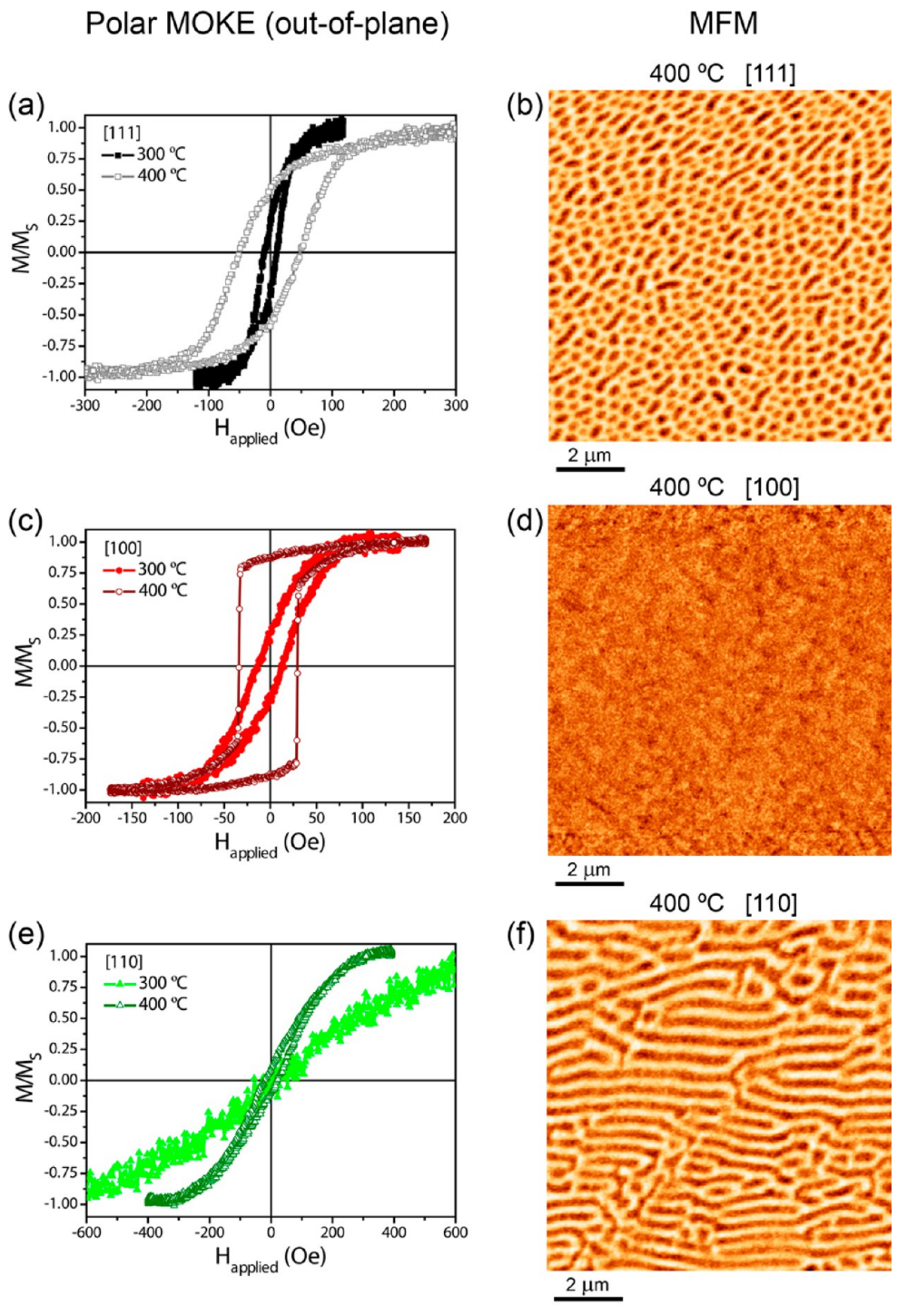

Figure 4. Out-of-plane magnetic properties of plasma-nitrided ASSs: (a), (c), and (e) are the polar MOKE loops corresponding to the [111], [100], and [110]-oriented expanded austenite produced at either 300 or 400 °C, respectively (the lines are guides for the eye only); (b), (d), and (f) are the MFM images taken at remanence after applying an out-of-plane magnetic field of 2000 Oe of the [111], [100], and [110] expanded austenite produced at 400 °C, respectively.

Magnetic force microscopy (MFM) has been used to further confirm the magnetic character of the samples processed at 400 °C and to unravel their magnetic configurations (Figure 4). The [100] sample shows virtually no contrast as expected from an almost single domain state in agreement with the high remanence obtained by polar MOKE (Table 2). In contrast, the [111] and [110]-oriented samples exhibit striped domains indicating a more complex magnetic structure. By determining the percentage of bright (P_S) and dark (P_D) areas of these MFM images, i.e., the fraction of magnetization pointing up or down (or vice versa), the remanences can be estimated as $P_S - P_D$. Specifically, the [111] and [110] samples show P_S values of around 76 and 56%, respectively. This corresponds to remanences of 52 and 12%, respectively, in excellent agreement with the remanences obtained by polar MOKE (Table 2), thus confirming the magnetometry results.

dx.doi.org/10.1021/am402773w | ACS Appl. Mater. Interfaces 2013, 5, 10118−10126

Table 2. Coercivity, H_C, and Remanence, Expressed as the Remanence Magnetization M_R Divided by the Saturation Magnetization M_S (M_R/M_S), of the Polar MOKE Hysteresis Loops of the Samples

sample		H_C [Oe]	M_R/M_S [%]
300 °C	[100]	13	27
	[110]	0	0
	[111]	10	28
400 °C	[100]	32	89
	[110]	21	10
	[111]	49	51

In-Plane Magnetic Characterization. In order to study the in-plane magnetic properties, hysteresis loops were acquired by longitudinal MOKE for various orientations of the samples with respect to the applied magnetic field (Figure 5). Note that 0° in Figure 5 corresponds to the in-plane measurements along the [$\bar{1}$11], [001], and [$\bar{1}$10] directions of the pristine [111], [100], and [110] ASS single crystals, respectively. Figure 5c,e shows the angular dependences of the remanence, expressed as M_R/M_S, and the coercivity, H_C, corresponding to the samples nitrided at 300 °C, respectively. For the [111]-oriented sample, the angular dependences of M_R/M_S and H_C suggest that nitriding at 300 °C results in a rather isotropic in-plane behavior. Conversely, for the [100] and [110] samples, a pronounced in-plane uniaxial (i.e., twofold) magnetic anisotropy is observed.

For samples prepared at 400 °C, the H_C is roughly of the same order for all orientations, while the M_R/M_S is significantly larger for the [100] sample (Figure 5b). Namely, for the [100] sample, while the angular dependence of the normalized remanence evidences a twofold anisotropy (i.e., two lobes, see Figure 5d), the polar plot of the coercivity indicates a fourfold

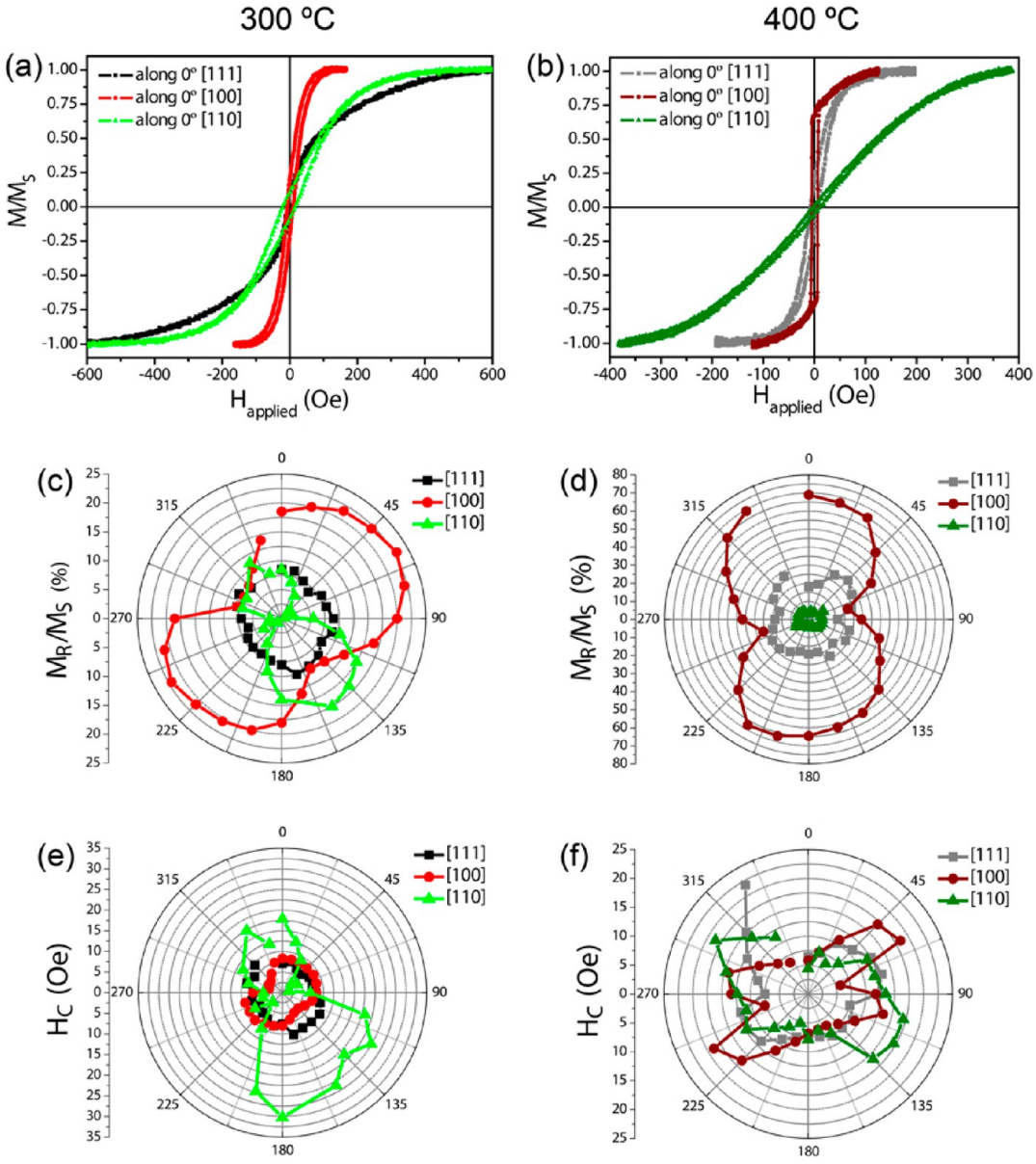

Figure 5. In-plane magnetic properties of plasma-nitrided ASSs: (a), (c), (e) and (b), (d), (f) are the longitudinal MOKE hysteresis loops along 0°, the in-plane angular dependences of the remanence (M_R/M_S), and the coercivity (H_C) for the samples processed at 300 and 400 °C, respectively. The lines are guides for the eye only.

anisotropy (i.e., four lobes, see Figure 5f). As can also be seen in Figure 5d,f, the angular dependences of M_R/M_S and H_C for the [111] expanded austenite exhibit a somewhat fourfold-like anisotropy. Conversely, less significant systematic features can be distinguished in the polar plots of the [110] sample prepared at 400 °C.

Correlation between Structural and Magnetic Properties. Nitriding at either 300 or 400 °C induces ferromagnetism via the formation of expanded austenite. At 300 °C, the [100]- and [111]-oriented samples do not have well established either easy or hard axes out-of-plane. Conversely, the significantly low remanence and coercivity of the polar MOKE measurement of the [110]-oriented sample suggest that the hard magnetic axis tends to lie along [110]. Interestingly, the samples prepared at 400 °C show an increased out-of-plane component (i.e., larger both coercivity and remanence) compared to the samples treated at 300 °C. Nitriding at either 300 or 400 °C results in rather unchanged out-of-plane apparent relative expansions for the [110] and [111] samples (Table 1). Moreover, the nitrogen content in the volume probed by MOKE can be roughly considered independent of both the processing temperature and the crystalline orientation. Thus, the enhanced out-of-plane contribution achieved at 400 °C might be ascribed to the expected formation of nanometric CrN precipitates at the near-surface.[7] While the small size or possible coherency does not allow for detectection of such precipitates by XRD,[30,31] their impact on the magnetic properties can be significant since they can effectively leave Fe- and Ni-enriched areas.[7] However, despite not being probed by MOKE, the larger N content below the near-surface of samples produced at 400 °C may also play a role in the enhanced out-of-plane contribution at the top surface. Furthermore, since CrN is antiferromagnetic with a bulk Néel temperature of about 280 K,[32] possible exchange interactions between CrN precipitates and Fe and/or Ni-enriched areas even above the Néel temperature of CrN might also contribute to the observed increase of H_C with processing temperature.[33] In particular, the [100] expanded austenite produced at 400 °C exhibits a rather square-shaped loop out-of-plane, suggesting the [100] direction as the magnetic easy axis in agreement with the XRD characterization, which reveals that the largest expansion in the direction normal to the surface occurs via the (200) planes of the [100]-oriented sample produced at 400 °C (Table 1). This is in agreement with the apparent tetragonal-like distortion along [100] of the [100]-oriented sample produced at 400 °C, which might result from the interplay among the in-plane biaxial residual stresses in the nitrided layer, the highly anisotropic mechanical behavior along (200) planes, the formation of nanometric CrN precipitates and probably the amount of incorporated nitrogen below the near-surface, creating a magnetic easy axis along the sample normal. Since the [100] direction is also the most expanded in the [110]-oriented sample, we can assume that its easy axis would still be in the [100] direction, although it would not be directed out-of-plane. Therefore, the loop for the [110] sample shows a reduced remanence with respect to that of the [100] sample. Even though this argument might also be applicable to the [111] sample, other easy axes cannot be ruled out since the out-of-plane expansion of (111) planes is similar to that of (100) planes (Table 1, Figure 4).

At 300 °C, the [111]-oriented sample exhibits a rather isotropic in-plane behavior, while a pronounced in-plane uniaxial (i.e., twofold) magnetic anisotropy is observed for the [100] and [110] samples for both the remanence and coercivity angular dependences. This is consistent with the higher atomic compaction of {111} planes with respect to that of {200} and {220}, which results in a more isotropic behavior. A uniaxial in-plane anisotropy might result from the interplay between the in-plane biaxial residual stresses in the nitrided layer and the anisotropy of the elastic constants. However, traces of the cubic symmetry of the crystalline structure, such as a biaxial (i.e., fourfold) contribution for the [100] sample, in the magnetic in-plane characterization should also be expected. Therefore, both the rather isotropic behavior of the [111] sample and the pronounced uniaxial character of the angular dependences of the [100] and [110] samples may imply that interstitial diffusion and stress relaxation via plastic deformation processes at 300 °C are still rather limited, leading to an expanded austenite with significant residual stress which may ultimately be responsible for the observed in-plane characteristics via residual stress effects in detriment of the expected cubic anisotropies in the $a-b$ plane. This is in agreement with the XRD patterns (Figure 1b) which show rather broad γ_N peaks originating from a widened distribution of lattice cell parameters and residual stresses. Nonetheless, it should be noted that this twofold magnetic anisotropy of the [100] and [110] samples is not fully uniaxial since the symmetry of the polar plots is broken (i.e., the lobes are not equal in size), which evidences a competition between uniaxial and, possibly, incipient cubic anisotropies due to the projected cubic symmetry in the $a-b$ plane.[34] A similar argument applies to the [111] sample since its in-plane behavior is not fully isotropic. In agreement with the out-of-plane characterization, no well-established in-plane easy axes are found for the samples produced at 300 °C.

Conversely, for the expanded phase obtained at 400 °C, the observations strongly suggest that the [100] directions constitute the in-plane easy axis. While H_C is roughly of the same order for all orientations, the M_R/M_S is significantly larger for the [100] sample (being the largest for the 0° measurement which is along [001]). For the [100] sample, the angular dependence of the normalized remanence evidences a twofold anisotropy (i.e., two lobes, Figure 5d), and the polar plot of the coercivity indicates a fourfold anisotropy (i.e., four lobes, Figure 5f). Moreover, a biaxial-like major contribution is also observed in the angular dependences of M_R/M_S and H_C for the [111] expanded austenite (Figure 5d,e, respectively). Actually, assuming that the easy axes should be along the ⟨100⟩ directions and taking into account the assumed cubic crystal symmetry of expanded austenite, the anisotropy expected for the [100] and [110] samples is biaxial (i.e., fourfold and 90° between lobes), while that of the [111] sample is triaxial (i.e., sixfold).[35] Even though complex angular dependences of the in-plane magnetic properties are envisaged for the [100] and [111] samples, experimental observations reveal that relaxation processes are enhanced at higher nitriding temperature, resulting in an expanded austenite with lower levels of residual stress and structural disorder than that at 300 °C. Such structural ordering consequently reinforces the in-plane projections of cubic anisotropies, such as the biaxial anisotropy contributions, in detriment of the uniaxial anisotropy ascribed to residual stress-induced effects. This is in agreement with the XRD analysis which shows sharper and more defined expanded austenite peaks (see Figure 1b) for samples prepared at 400 °C than at 300 °C. Concomitantly, a certain role of the CrN formation in the strengthening of the biaxial anisotropy with

temperature could be also envisaged since areas rich in Fe and/or Ni are expected.

Concerning the [110] sample prepared at 400 °C, no traces of significant in-plane systematic features can be distinguished in the polar plots. This might evidence that lattice rotation occurs for this orientation, in concordance with the low intensity of its XRD lines and the increased misorientation with its parent austenite (Figures 1b and 2, respectively). Thus, the related dependence of magnetic properties on specific orientations is less precise and not so well-defined.

Finally, it is worth mentioning that, whereas the easy magnetic axis lies down along basic directions (i.e., [100]) in single crystalline expanded austenite produced at 400 °C, that of polycrystalline expanded austenite obtained using similar conditions can take unusual directions.[13] This strongly suggests that the interplay among magnetocrystalline anisotropy and exchange, dipolar, and mechanical interactions between grains plays a significant role in determining the effective magnetic properties of polycrystalline expanded austenite, concealing to some extent the effect of the N surface concentration and corresponding lattice expansion.

CONCLUSIONS

A correlation between the structural and magnetic properties of single crystalline [100]-, [110]-, and [111]-oriented expanded austenite has been carried out. Symmetric and asymmetric X-ray diffraction scans reveal the single crystalline character of the different γ_N samples. The results are consistent with a stressed and faulted FCC structure with a slight tetragonal-like distortion along [100] in the [100]- and [110]-oriented samples. The magnetic characterization indicates that, whereas no clear easy axis exists in the samples processed at 300 °C, the [100] direction constitutes the easy axis for the γ_N phase produced at 400 °C. This is mainly linked to the interplay between an increased lattice cell expansion and the expected formation of nanometric CrN precipitates, effectively resulting in Fe- and Ni-enriched areas. The combination of uniaxial anisotropies (probably due to in-plane residual stresses) and cubic anisotropies, such as biaxial anisotropy, inherent to the cubic symmetry in the $a-b$ plane results in rather complex in-plane magnetic properties. However, with processing temperature, the biaxial in-plane anisotropy strengthens in detriment of the uniaxial contribution in agreement with a more homogeneous structure of expanded austenite (i.e., a more effective accommodation of stresses via plastic deformation at 400 °C than at 300 °C). The absence of mechanical and magnetic grain to grain interactions eases the analysis and allows assuming that the lattice expansion and the expected formation of CrN precipitates are the main factors for establishing the easy axis along simple directions in single crystalline expanded austenite produced at 400 °C.

EXPERIMENTAL SECTION

316L ASS bulk single crystals with [111], [100], and [110] crystalline orientations have been plasma-nitrided for 60 min at either 300 or 400 °C in a home-made reactor with the samples at plasma potential[36] (details on sample preparation and plasma conditions are reported elsewhere).[25] Quantitative nitrogen depth profiles have been determined by nuclear reaction analysis (NRA) using the $^{14}N(d,\alpha)^{12}C$ nuclear reaction at an incident deuterium energy of 1.4 MeV. The nitrided surface layers (i.e., expanded austenite γ_N) have been structurally investigated by X-ray diffraction (XRD) with Cu $K\alpha_1$ radiation, using either symmetric or asymmetric $\theta/2\theta$ scans. In order to unravel the mutual orientation between the substrate and the nitrided top layers, asymmetric Φ scans (where Φ is the azimuthal angle) have been carried out while varying χ (i.e., the sample is tilted over an angle χ with respect to its surface in order to align the atomic planes of interest perpendicularly to the scattering plane) to obtain the pole figures. Finally, ω scans (i.e., rocking curves) have been performed to assess the mosaic spread of both the parent γ austenite and the formed γ_N expanded austenite phases. XRD measurements were carried out using a Panalytical X'Pert PRO MRD diffractometer equipped with a 0.04 radian Soller slit, a 2 mm mask, and a 1/2° fixed divergence slit to monitor the incident beam and a 0.27° parallel plate collimator for the diffracted beam. The out-of-plane and in-plane magnetic properties have been characterized by polar and longitudinal magneto-optical Kerr effect (MOKE), respectively, while magnetic force microscopy (MFM) served to image the magnetic domain configurations.

AUTHOR INFORMATION

Corresponding Authors

*E-mail: enric.menendezdalmau@fys.kuleuven.be (Enric Menéndez).

*E-mail: claude.templier@univ-poitiers.fr (Claude Templier).

Notes

The authors declare no competing financial interest.

ACKNOWLEDGMENTS

This work was financed by the Fund for Scientific Research-Flanders (FWO), the KU Leuven Concerted Action (GOA/09/006 and GOA/14/007) programs, the 2009-SGR-1292 project of the Generalitat de Catalunya, and the MAT2010-20616-C02 project of the Spanish Ministerio de Economía y Competitividad. The authors acknowledge Dr. Gintautas Abrasonis and Dr. Frans Munnik, from Helmholtz-Zentrum Dresden-Rossendorf, (Dresden, Germany), for the assistance with NRA experiments and NRA data processing. E.M. thanks the Fund for Scientific Research-Flanders (FWO) for financial support.

REFERENCES

(1) Menéndez, E.; Sort, J.; Liedke, M. O.; Fassbender, J.; Suriñach, S.; Baró, M. D.; Nogués, J. *J. Mater. Res.* **2009**, *24*, 565−573.

(2) Sort, J.; Concustell, A.; Menéndez, E.; Suriñach, S.; Baró, M. D.; Farran, J.; Nogués, J. *Appl. Phys. Lett.* **2006**, *89*, 032509.

(3) Hecker, S.; Stout, M.; Staudhammer, K.; Smith, J. *Metall. Mater. Trans.* **1982**, *13*, 619−626.

(4) Öztürk, O.; Williamson, D. L. *J. Appl. Phys.* **1995**, *77*, 3839−3850.

(5) Basso, R. L. O.; Pimentel, V. L.; Weber, S.; Marcos, G.; Czerwiec, T.; Baumvol, I. J. R.; Figueroa, C. A. *J. Appl. Phys.* **2009**, *105*, 124914.

(6) Dong, H. *Int. Mater. Rev.* **2010**, *55*, 65−98.

(7) Martinavičius, A.; Abrasonis, G.; Scheinost, A. C.; Danoix, R.; Danoix, F.; Stinville, J. C.; Talut, G.; Templier, C.; Liedke, O.; Gemming, S.; Möller, W. *Acta Mater.* **2012**, *60*, 4065−4076.

(8) Richter, E.; Günzel, R.; Parascandola, S.; Telbizova, T.; Kruse, O.; Möller, W. *Surf. Coat. Technol.* **2000**, *128-129*, 21−27.

(9) Bell, T. *Surf. Eng.* **2002**, *18*, 415−422.

(10) Menéndez, E.; Martinavicius, A.; Liedke, M. O.; Abrasonis, G.; Fassbender, J.; Sommerlatte, J.; Nielsch, K.; Suriñach, S.; Baró, M. D.; Nogués, J.; Sort, J. *Acta Mater.* **2008**, *56*, 4570−4576.

(11) Menéndez, E.; Stinville, J.-C.; Tromas, C.; Templier, C.; Villechaise, P.; Rivière, J.-P.; Drouet, M.; Martinavicius, A.; Abrasonis, G.; Fassbender, J.; Baró, M. D.; Sort, J.; Nogués, J. *Appl. Phys. Lett.* **2010**, *96*, 242509.

(12) Martinavičius, A.; Abrasonis, G.; Möller, W.; Templier, C.; Rivière, J. P.; Declémy, A.; Chumlyakov, Y. *J. Appl. Phys.* **2009**, *105*, 093502.

(13) Abrasonis, G.; Riviere, J. P.; Templier, C.; Declemy, A.; Pranevicius, L.; Milhet, X. *J. Appl. Phys.* **2005**, *97*, 083531.

(14) Abrasonis, G.; Rivière, J. P.; Templier, C.; Declémy, A.; Muzard, S.; Pranevicius, L. *Surf. Coat. Technol.* **2005**, *196*, 262−266.
(15) Martinavicius, A.; Abrasonis, G.; Moeller, W. *J. Appl. Phys.* **2011**, *110*, 074907.
(16) Abrasonis, G.; Möller, W.; Ma, X. *Phys. Rev. Lett.* **2006**, *96*, 065901.
(17) Sun, Y.; Li, X. Y.; Bell, T. *J. Mater. Sci.* **1999**, *34*, 4793−4802.
(18) Xu, X.; Yu, Z.; Wang, L.; Qiang, J.; Hei, Z. *Surf. Coat. Technol.* **2003**, *162*, 242−247.
(19) Birkholz, M. In *Thin Film Analysis by X-Ray Scattering*; Wiley-VCH: Weinheim, 2006; p 278.
(20) http://physics.nist.gov/PhysRefData/XrayMassCoef/tab3.html (accessed Oct. 5, 2013).
(21) Hoeft, D.; Latella, B. A.; Short, K. T. *J. Phys.: Condens. Matter* **2005**, *17*, 3547−3558.
(22) Manova, D.; Günther, C.; Bergmann, A.; Mändl, S.; Neumann, H.; Rauschenbach, B. *Nucl. Instrum. Methods Phys. Res., Sect. B* **2013**, *307*, 310−314.
(23) Christiansen, T.; Somers, M. A. J. *Metall. Mater. Trans. A* **2006**, *37*, 675−682.
(24) Stinville, J. C.; Villechaise, P.; Templier, C.; Rivière, J. P.; Drouet, M. *Acta Mater.* **2010**, *58*, 2814−2821.
(25) Templier, C.; Stinville, J. C.; Villechaise, P.; Renault, P. O.; Abrasonis, G.; Rivière, J. P.; Martinavicius, A.; Drouet, M. *Surf. Coat. Technol.* **2010**, *204*, 2551−2558.
(26) Mingolo, N.; Tschiptschin, A. P.; Pinedo, C. E. *Surf. Coat. Technol.* **2006**, *201*, 4215−4218.
(27) Fewell, M. P.; Priest, J. M. *Surf. Coat. Technol.* **2008**, *202*, 1802−1815.
(28) Grigull, S.; Parascandola, S. *J. Appl. Phys.* **2000**, *88*, 6925−6927.
(29) Christiansen, T. L.; Hummelshøj, T. S.; Somers, M. A. J. *Surf. Eng.* **2010**, *26*, 242−247.
(30) Oddershede, J.; Christiansen, T. L.; Ståhl, K.; Somers, M. A. J. *Scr. Mater.* **2010**, *62*, 290−293.
(31) Oddershede, J.; Christiansen, T. L.; Ståhl, K.; Somers, M. A. J. *J. Mater. Sci.* **2008**, *43*, 5358−5367.
(32) Alling, B. *Phys. Rev. B* **2010**, *82*, 054408.
(33) Leighton, C.; Suhl, H.; Pechan, M.; Compton, R.; Nogués, J.; Schuller, I. K. *J. Appl. Phys.* **2002**, *92*, 1483−1488.
(34) Ecija, D.; Jiménez, E.; Camarero, J.; Gallego, J. M.; Vogel, J.; Mikuszeit, N.; Sacristán, N.; Miranda, R. *Phys. Rev. B* **2008**, *77*, 024426.
(35) Du, H.-F.; He, W.; Liu, H.-L.; Fang, Y.-P.; Wu, Q.; Zou, T.; Zhang, X.-Q.; Sun, Y.; Cheng, Z.-H. *Appl. Phys. Lett.* **2010**, *96*, 142511.
(36) Perrière, J.; Siejka, J.; Rémili, N.; Laurent, A.; Straboni, A.; Vuillermoz, B. *J. Appl. Phys.* **1986**, *59*, 2752−2759.